

Article

Evolution and Near-Wall Effect of the Vortex Structures Induced by In-Line Twin Synthetic Jets in a Crossflow

Hongxin Wang^{1,2}, Degang Xu^{1,*}, Linwen Li², Kaiwen Zhou³, Xin Wen^{3,*} and Hui Tang⁴¹ School of Automation, Central South University, Changsha 410083, China² Shanghai Aircraft Design and Research Institute, Shanghai 201210, China³ Key Lab of Education Ministry for Power Machinery and Engineering, School of Mechanical Engineering, Shanghai Jiao Tong University, 800 Dongchuan Road, Shanghai 200240, China⁴ Department of Mechanical Engineering, The Hong Kong Polytechnic University, Kowloon, Hong Kong, China

* Correspondence: dgxu@csu.edu.cn (D.X.); wenxin84@sjtu.edu.cn (X.W.)

Abstract: This paper aims to further the understanding of the mixing process of in-line twin synthetic jets (SJs) and their impact in the near-wall region in a flat-plate laminar boundary layer. A numerical study has been carried out, in which colored fluid particles and the Q criterion are used to track the SJ-induced vortex structures at the early stage of the evolution. Interacting vortex structures at four selected phase differences are presented and analyzed. It is found that the fluid injected at the early stage of the blowing stroke mainly contributes to the formation of the hairpin legs, the fluid injected near the maximum blowing mainly contributes to the formation of the hairpin head, and the fluid injected at the late stage of the blowing stroke contributes very little to the formation of the hairpin vortex. It is also confirmed that, irrespective of the phase difference, the hairpin vortex issued from the upstream actuator is more capable of maintaining its coherence than its counterpart issued from the downstream actuator. The influence of the interacting vortex structures on the boundary layer is also studied through investigating excess wall shear stress. In all cases, a pair of streaks of high wall shear stress can be observed with similar size. Among them, the streaks have the strongest wall shear stress, with the largest gap at phase difference 0 when partially interacting vortex structures are produced. The findings can provide valuable guiding information for the applications of synthetic jets in heat transfer, mixing control, and flow control in a crossflow.

Keywords: twin synthetic jets; laminar boundary layer; vortex interaction; simulation

Citation: Wang, H.; Xu, D.; Li, L.; Zhou, K.; Wen, X.; Tang, H. Evolution and Near-Wall Effect of the Vortex Structures Induced by In-Line Twin Synthetic Jets in a Crossflow. *Actuators* **2022**, *11*, 234. <https://doi.org/10.3390/act11080234>

Academic Editor: André Preumont

Received: 22 July 2022

Accepted: 12 August 2022

Published: 16 August 2022

Publisher's Note: MDPI stays neutral with regard to jurisdictional claims in published maps and institutional affiliations.



Copyright: © 2022 by the authors. Licensee MDPI, Basel, Switzerland. This article is an open access article distributed under the terms and conditions of the Creative Commons Attribution (CC BY) license (<https://creativecommons.org/licenses/by/4.0/>).

1. Introduction

A synthetic jet (SJ) actuator can produce a train of vortical structures by the periodical motion of an oscillatory diaphragm on a cavity [1–3]. These vortical structures can effectively enhance fluid mixing in the crossflow, thereby providing an effective mechanism of boundary layer flow control [4–9].

Previous works were carried out to investigate the impact of the SJ-induced vortical structures in the near-wall region of a boundary layer, where effective flow separation control and wall heat transfer are ultimately desired. Using dye visualization, Zhong et al. [10] and Jabbar and Zhong [11] looked at more detailed interactions and identified three key SJ-induced vortex structures, i.e., hairpin vortices, stretched vortex rings, and tilted vortex rings, under different jet operation and boundary layer flow conditions. Different thermal footprints on the wall are correlated to the vortical structures induced by SJs. Using high-frame-rate particle image velocimetry (PIV) experiments, Jabbar and Zhong [12] confirmed that the wall shear stress shares similar patterns with the thermal footprints, and found that hairpin vortices and stretched vortex rings are able to offer enhanced heat transfer in the near-wall region. Using numerical methods, Lee et al. [13] confirmed the effective wall cooling of single SJs in micro-channels. They also found that

the flow structures induced by stronger SJs in the micro-channel can exert larger mixing regions and stronger convection at the heated wall surface.

To increase the impact region, SJ arrays are usually applied. For example, in the application of fluid cooling, Lee et al. [14] found that twin SJs in out-of-phase operation can significantly enhance wall surface cooling due to the enhanced fluid mixing. However, unlike single SJs, the interactions between multiple circular SJs and cross-flows, as well as among multiple SJs, have not been fully studied and understood. Very limited investigations have been reported on this topic in the literature, especially on the near-wall effect. Based on oil visualization, Watson et al. [15] examined the in-interaction of two neighboring SJs in a boundary layer flow, and pointed out that the twin SJs can perform in either a constructive (enhancing the strength of the SJs) or a destructive (weakening the SJs) manner under different configurations. Using hot-wire measurements, Liddle and Wood [16] and Liddle et al. [17] confirmed that the phase difference plays a very important role in the interaction of twin SJs in a crossflow. At a 2700 phase difference, the SJ actuators in the upstream and downstream locations yielded a more concentrated movement of near-wall fluid towards the vortex core than at a 900 phase difference. With PIV measurements of in-line twin SJs in a channel flow, Honami and Motosuke [18] found that the twin SJs can have different vortex strengths with different configurations. Although these studies revealed useful physical insights, they are not enough to give a holistic picture of the flow structures induced by multiple circular SJs in a crossflow and their near-wall effect. Therefore, more detailed studies are highly desired.

Although these works have revealed some useful physical insights into the interaction of in-line twin SJs in boundary layers, the detailed vortex interaction and evolution of twin SJs are not well understood. Limited by the spatial and temporal resolution, it is difficult for current experimental methods to capture the three-dimensional flow structures of twin SJs. In addition, it is also difficult to examine the evolution of the interacting flow structure issued from different SJ actuators in Cartesian coordinates. Therefore, two research questions still remain: First, how does the mixing process of the twin-SJ-induced flow structures occur in detail? Second, what is the influence of these flow structures on the boundary layer flow, especially in the near-wall region? By examining the flow structures and their impact in the boundary layer, we can obtain results which are valuable for flow control and heat transfer applications. For example, strong vortices and high wall shear stress can produce high flow mixing in the boundary layer, delaying flow separation and enhancing heat transfer on the wall. Therefore, to address these questions in the present research, a numerical study is conducted. A cluster of colored fluid particles are used to track the evolution and mixing process of the single and twin SJs at the early stage. In the Lagrangian perspective, fluid particles are applied to examine the flow dynamical system rather than a continuum [19]. It is widely used to present high-quality visible details of time-dependent vortex structures, which may not be apparent in the classical Eulerian fields [20,21]. In addition, to capture the associated vortex structures, Q iso-surfaces are defined [22]. Finally, the excess wall shear stress is evaluated and compared.

2. Methodology

2.1. Problem Description

The twin SJ actuators used in the present numerical study are identical to those used in our previous experiment [23,24]. The SJ cavity has an orifice with a diameter of $D_o = 5$ mm. The centers of the two SJ actuator orifices are at a distance of $d = 10$ mm. Similar to previous experiments [23], the oscillation diaphragm of each actuator has a diameter of $D_d = 45$ mm, which oscillates like a piston, with velocity varying in a sinusoidal manner.

$$u_d(t) = \pi\Delta f \sin(2\pi ft) \quad (1)$$

where Δ is the peak-to-peak displacement of the diaphragm and f the oscillation frequency. During an actuation cycle, the beginning of blowing is defined as $t/T = 0$ (and 1). In the

present study, the working flow is water, which is incompressible. According to Tang and Zhong [25], the jet velocity \bar{U}_o averaged over an entire actuation cycle can be calculated as

$$\bar{U}_o = \frac{1}{T} \int_0^{T/2} u_o(t) dt = \Delta f \left(\frac{D_d}{D_o} \right)^2 \quad (2)$$

where the instantaneous jet velocity is $u_o(t)$.

In current study, the bulk flow has a velocity of $U_\infty = 0.055$ m/s. The bulk flow has a boundary layer thickness of 15 mm, i.e., $\delta = 3D_o$, at the actuator orifices. Based on Reynolds number, the momentum thickness is $Re_\theta \approx 106$. The actuators have a diaphragm displacement of $\Delta = 0.158$ mm with a frequency of $f = 1$ Hz. To characterize the performance of SJs in a laminar boundary layer, the dimensionless stroke length L and velocity ratio VR are also defined according to Wen and Tang [24]. The stroke length L is defined as

$$L = \frac{L_o}{D_o} = \frac{\bar{U}_o}{fD_o} \quad (3)$$

where L_o is the jet column length during the SJ blowing stroke. The jet strength is characterized by the velocity ratio VR as

$$VR = \frac{\bar{U}_o}{U_\infty} \quad (4)$$

From Equations (2)–(4), the settings in the present study yield $L = 2.6$ and $VR = 0.23$, to produce hairpin vortices according to the parametric map revealed by Jabbar & Zhong [11]. These hairpin vortices can stay in the boundary layer and hence are very desired in SJ-based flow separation delay.

In the present study, the two SJ actuators are arranged in line with the crossflow and are separated by a fixed distance $d = 2D_o$. Phase difference between the two SJs are investigated by $\Delta\phi = 0, \pi/2, \pi$ and $3\pi/2$ (or $-\pi/2$). Here $\Delta\phi = 0$ means that the twin SJs are in phase, and the $\Delta\phi = \pi/2$ means the downstream actuator is $\pi/2$ behind, and so on.

2.2. Numerical Approaches

Figure 1 shows the computational geometry and boundary conditions, which are similar to those used in Wen and Tang [26] and Zhou and Zhong [27]. In the x (streamwise) direction, the simulation domain has a length of $55D_o$. In the y (wall-normal) and z (spanwise) directions, the domain is $30D_o$ and $20D_o$, respectively. The origin of the coordinate system is set at the midpoint of two actuator orifice centers, which are $15D_o$ downstream from the crossflow inlet. Although not presented in Figure 1, the cavities of the two SJ actuators are included in the simulation. The crossflow in-let on the left of the computational domain is set as the velocity inlet with a laminar Blasius velocity profile. The wall of flat plate in the boundary layer and the SJ actuators are set as no-slip conditions. Both lateral sides of the crossflow domain are set as periodic conditions. The upper face and the downstream boundary on the right of the crossflow domain are set as the pressure outlet. On the diaphragms of the actuators, a time-dependent velocity condition is set according to Equation (1).

To activate the SJ actuator, the motion of the diaphragm in the cavity is controlled by setting a time-dependent velocity boundary condition according to Equation (1). In this study, water is used, which is incompressible. The fluid is governed by mass conservation and momentum conservation. The flow is laminar; therefore, no turbulent model is used. The second-order implicit scheme is used in time, and the second-order upwind scheme is used in space. For the pressure–velocity coupling, the pressure-implicit with splitting of operators method is used. The unsteady, three-dimensional incompressible Navier–Stokes equations are solved by a commercial CFD code, ANSYS FLUENT 2020 R2.

$$\frac{\partial u_i}{\partial x_i} = 0 \quad (5)$$

$$\frac{\partial u_i}{\partial t} + u_j \frac{\partial u_i}{\partial x_j} = -\frac{1}{\rho} \frac{\partial p}{\partial x_i} + \nu \frac{\partial^2 u_i}{\partial x_j \partial x_j} \tag{6}$$

where ρ is the fluid density and ν is viscosity, and the summation notion is applied. Sensitivity studies have been conducted to ensure the mesh number and time-step size are optimum. Three different mesh numbers, i.e. 2.1×10^6 , 2.8×10^6 , and 3.7×10^6 , and three different time-step sizes, i.e. $1/240$ s, $1/360$ s, and $1/480$ s, are examined. Mesh and time sensitivity studies have been conducted for the case of twin SJs operating in phase (i.e., $\Delta\phi = 0$). With different mesh sizes and time steps, the time-averaged velocity profiles along a spanwise, wall-parallel line (i.e., $x/D_o = 5$ and $y/D_o = 2$) within the boundary layer are compared. As shown in Figure 2, the simulation result seems independent of the selected mesh size and time step, confirming the mesh and time convergence in the current study. The total number of meshes used in the simulation is about 2.8 million. In one diaphragm oscillation cycle, there are 240 time steps as a compromise between computational accuracy and time.

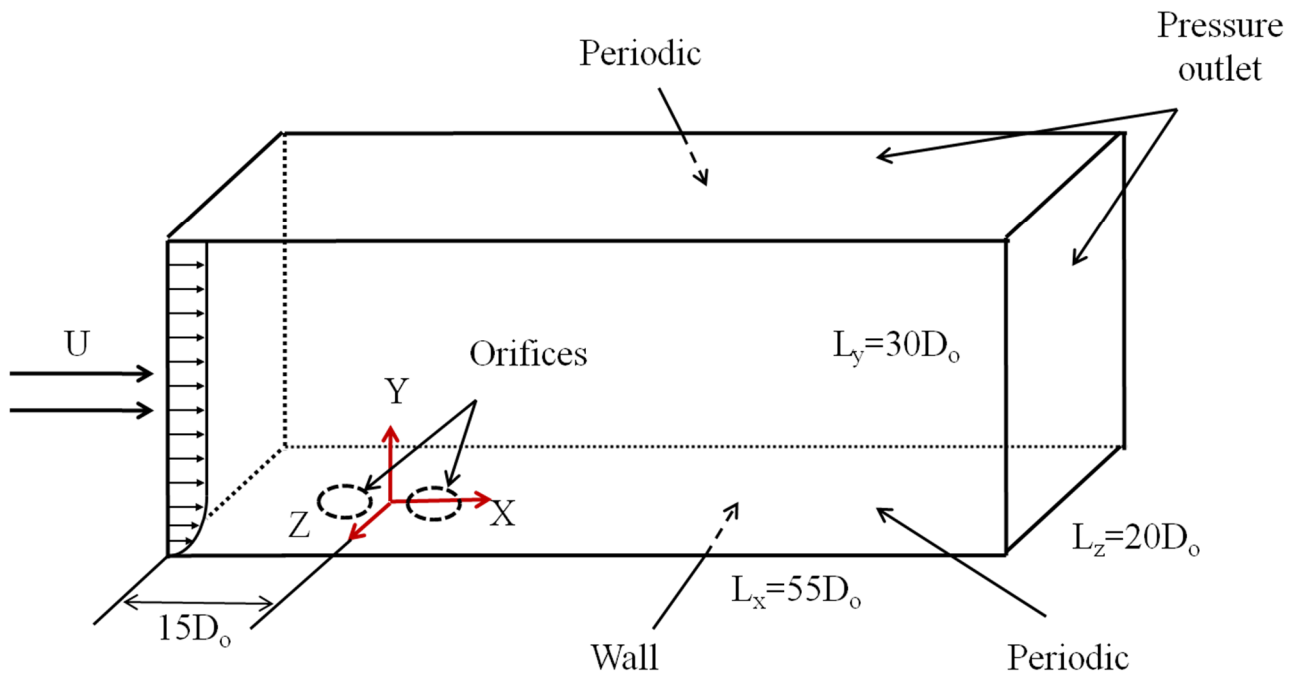


Figure 1. Computational geometry and boundary conditions for current CFD simulations. The actuator cavities are included in the simulation (although the cavities are not presented). The orifices of the two actuators are presented as dash circles located close to the origin of the coordination.

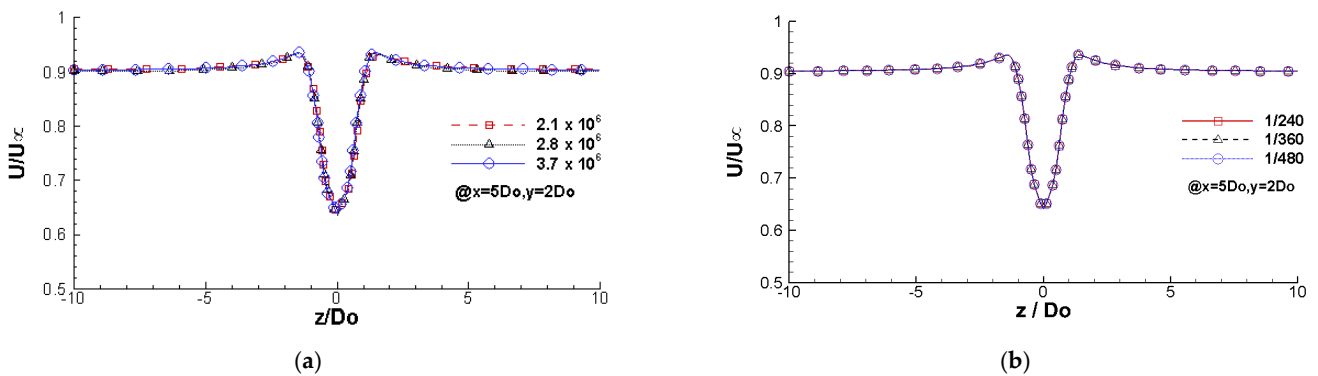


Figure 2. Comparison of the time-averaged velocity profiles along a spanwise, wall-parallel line (i.e., $x/D_o = 5$ and $y/D_o = 2$) within the boundary layer for the (a) mesh size (chosen value 2.8×10^6) and (b) time step (chosen value $1/240$) sensitivity studies for the twin SJs operating in phase.

In the present study, the SJ-induced vortex structures are identified using the Q criterion [22]. A vortex structure can be captured by an iso-surface of a positive Q value. To differentiate individual SJs in the present simulation, particles of two different colors are continuously and uniformly released from the two actuator orifices during the blowing cycle once the flow field reaches its steady state. The density of these particles is set to that of water, and the discrete particle model (DPM) is used to track them. Similar to our dye visualization experiment [23,24], the particles issued from the upstream actuator are colored in red, whereas those from the downstream actuator are in green.

To reflect the capability of the SJ-induced vortex structures in flow separation control, wall shear stress is calculated based on the least squares cell-based gradient discretization proposed by Anderson and Bonhaus [28] to ensure a second-order interpolation, with a spatial resolution of 0.5% of the boundary layer thickness or $y^+ = 0.2$.

2.3. Validation

The present CFD framework has been well validated with a single SJ in our previous work [26]. To further validate this framework for the current twin-SJ configuration, experiments are conducted using color dye visualization and PIV measurement. In dye visualization, food dye with two different colors fills the two actuator cavities, i.e. red color for the upstream actuator and green color for the downstream. Methanol is premixed with the dye to achieve a similar density to water. Two cameras are used to capture images from the side and bottom views. In the PIV measurement, the Dantec system is used. Polyamide seeding particles are used to track the flow, and a FlowSense 2M charge-coupled-device camera is used to capture the particle images. A double pulsed Nd:YAG laser is used to illuminate the seeding particles. The sampling frequency of PIV measurement is 10 Hz. For each case, 300 image pairs are taken to achieve convergence. The PIV measurement results are verified with Blasius solution. More details of the dye visualization and PIV measurement can be found in our previous work [23]. To validate the CFD framework, flow patterns represented by colored fluid particles in the simulation are first compared to those in the color dye visualization experiment. As shown in Figure 3, the simulated particle patterns match with the dye visualization in a good manner. As shown in Figure 4, instantaneous and time-averaged velocity profiles are also compared at $x = 4D_o$, with a good agreement between the simulation results and the PIV data.

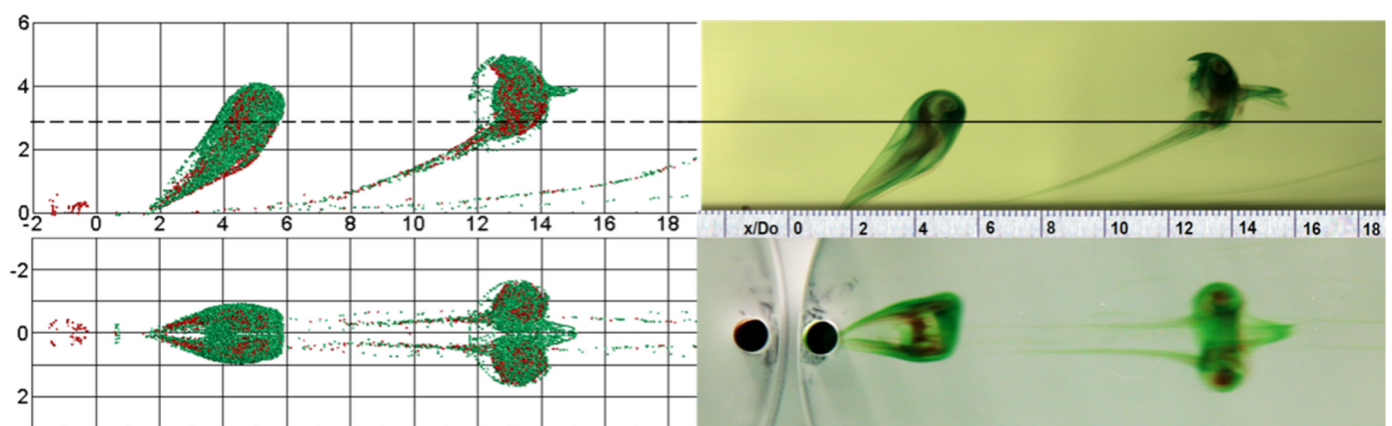


Figure 3. CFD Particle patterns (left) and experimental dye visualization (right) for the twin SJs at $\Delta\phi = \pi/2$ and $t/T = 0.25$ (The lines indicate the edge of the boundary layer).

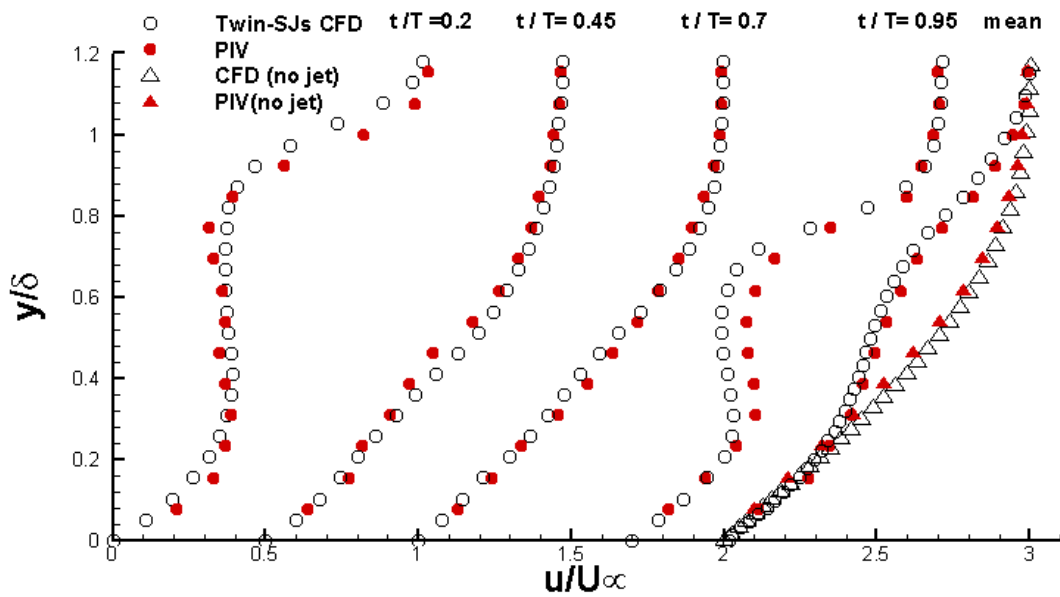


Figure 4. Comparison of instantaneous and time-averaged streamwise velocity profiles taken at $x = 4D_o$ from the CFD and PIV data for twin SJs operating at $\Delta\phi = 0$. The $t/T = 0.45, 0.7, 0.95$ profiles and the mean profile are shifted by $u/U_\infty = 0.5, 1.0, 1.7$ and 2 , respectively.

3. Evolution and Interaction of In-Line Twin SJ-Induced Flow Structures

3.1. Flow Structures of a Single SJ in a Crossflow

The single-SJ-induced flow structures visualized by the fluid particles, and the Q iso-surfaces are presented first to serve as the baseline case. As shown in Figure 5a, iso-surfaces of $Q = 5$ are superimposed over the particles, showing that the flow structures represented by the fluid particles coincide with the primary hairpin vortices captured by the Q iso-surfaces in terms of the shape, size, and location. This confirms that, in addition to the Q iso-surfaces, the SJ-induced hairpin vortices can also be examined through the pattern and motion of fluid particles. As shown in Figure 5b, where only the fluid particles are presented, each hairpin vortex is well represented by a strong head and a pair of slim, stretched legs. The hairpin head also carries a spiral of fluid particles when seen from the side cross-section view, indicating very strong rotation inside. However, no particles are observed in the induced secondary vortices that are captured by the Q iso-surfaces as shown in Figure 5a. This is not surprising because the particles are all released from the actuator orifice, while the secondary vortices form with ambient fluid that does not carry any particles. These secondary vortices are very close to the wall and hence play an important role in SJ-related flow separation control [26].

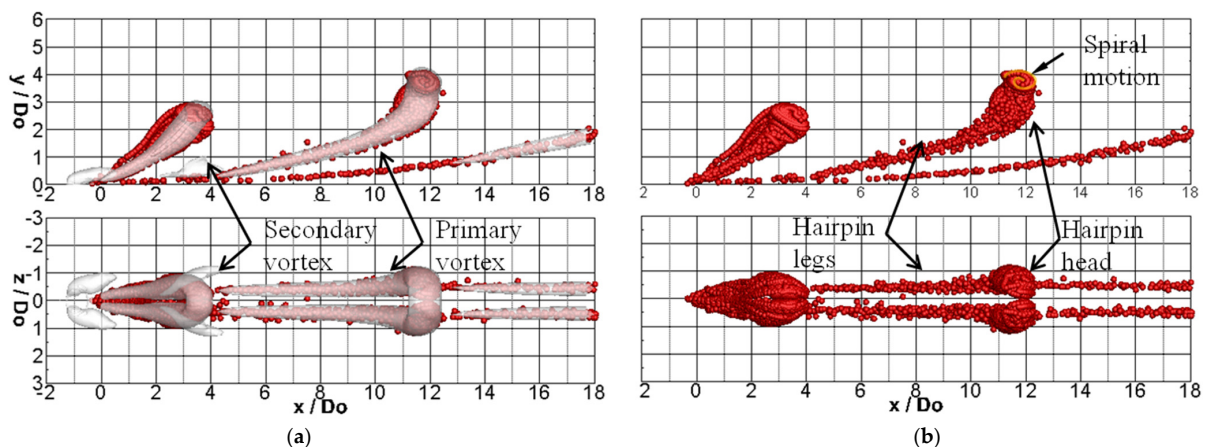


Figure 5. (a) Fluid particles plus $Q = 5$ iso-surfaces and (b) fluid particles for a single SJ at $t/T = 0$.

3.2. Evolution of Single and In-Phase Twin SJs

By using a sequence of snapshots of fluid particles, the evolution of the single SJ is presented in the upper two rows of Figure 6. It can be seen that, after expulsion from the actuator, the SJ-induced vortex ring gradually tilts downstream because of the velocity gradient in the boundary layer. Its upstream part is weakened by the boundary layer. As time advances, a hairpin vortex is formed by the shear stress in the boundary layer. It should be noted that the hairpin vortex is formed in a boundary layer with a flat plate. The wall-surface shape and obstacles in the boundary layer can significantly affect the evolution of hairpin vortices and horseshoe vortices, which is comprehensively discussed in previous works [29–31]. To further reveal the contribution of various SJ portions to the resulting hairpin vortex, three groups of fluid particles are marked in the snapshots, which are released from the orifice exit at three consecutive instants, i.e., $t = 0.0625T$ (group one), $0.25T$ (group two), and $0.4375T$ (group three). Each group consists of four selected particles, representing the upstream, central, downstream, and side portions of the SJ cross-section, respectively. By tracking these three groups of particles, it is found that the hairpin head contains fluid particles mainly from group two, while the hairpin legs contain fluid particles mainly from group one. As for the fluid particles in group three, most of them are inhaled back into the actuator during the SJ ingestion process ($t = 0.5T \sim T$). This result indicates that the fluid injected at the early stage of the blowing stroke ($t \approx 0$) mainly contributes to the formation of hairpin legs, the fluid injected near the maximum blowing ($t \approx 0.25T$) mainly contributes to the formation of the hairpin head, and the fluid injected at the late stage of the blowing stroke ($t \approx 0.5T$) contributes very little to the formation of the hairpin vortex.

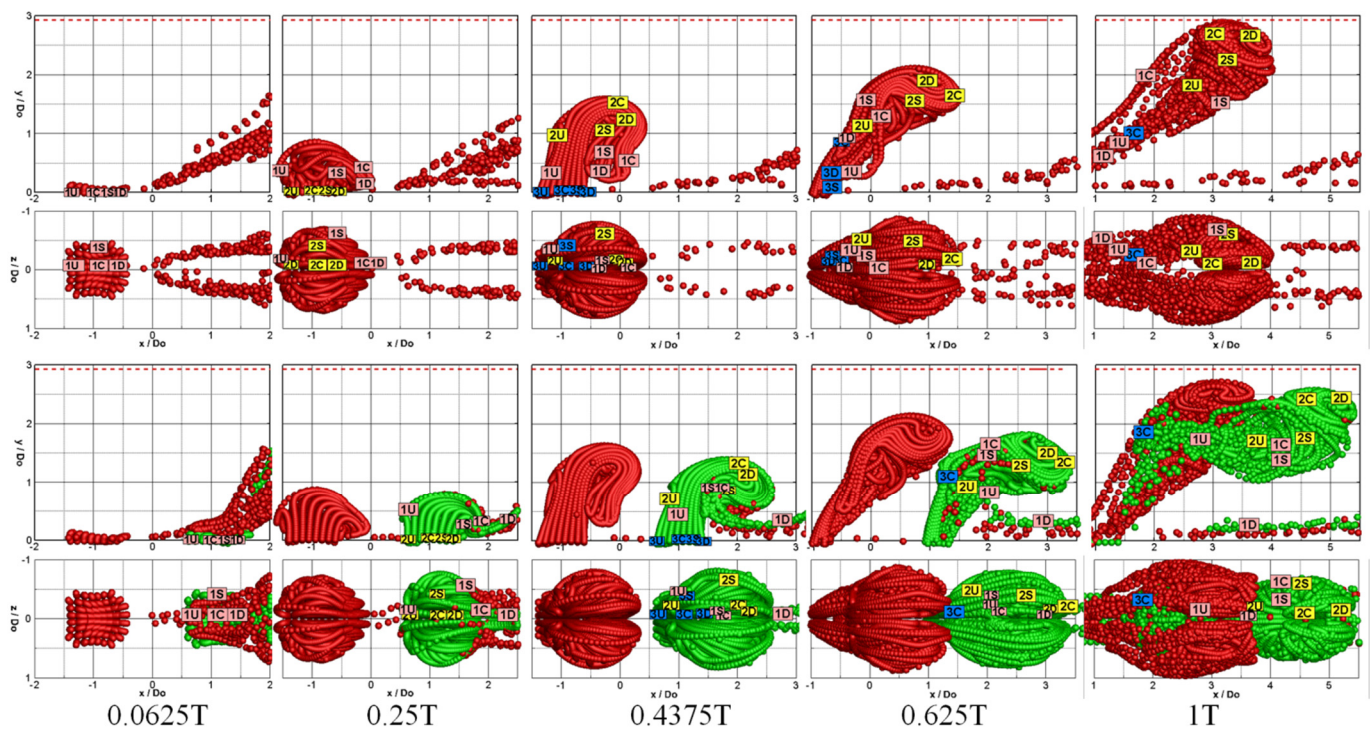


Figure 6. Evolution of fluid particles of the single SJ (upper two rows) and in-phase twin SJs (lower two rows). Group 1 particles (in pink) are released at $t/T = 0.0625$, Group 2 particles (in yellow) are released at $t/T = 0.25$, and Group 3 particles (in blue) are released at $t/T = 0.4375$. All particles are released at the actuator orifice exit.

If another SJ is introduced near the single SJ, the interaction between these two SJs will result in the formation of new flow structures. Take the in-phase, in-line twin SJs as an example, whose evolution is presented in the lower two rows of Figure 6. The SJ issued from the upstream actuator (in red, also called the trailing vortex in this case) is similar to

the single SJ before it entrains its downstream counterpart, while the SJ issued from the downstream actuator (in green, also called the leading vortex) is significantly affected by its upstream counterpart. The interaction between these two SJs is evidenced by the lift-up of the leading vortex legs and their entrainment into the trailing vortex. Furthermore, since it is the leading vortex that is significantly affected by the interaction, the same three groups of fluid particles as in the single-SJ case are released from the downstream orifice exit. By tracking these particles and comparing their traces with those in the single SJ, it can be seen that during the blowing stroke ($t = 0 \sim 0.5T$), the evolution of these particles is similar to that in the single-SJ case, except that the particles released from the downstream portion of the SJ cross-section at the early stage of the blowing stroke (marked as “1D”) are stripped out from the main vortex structure under the influence of the preceding vortices. When the twin SJs start interacting with each other in the ingestion period ($t = 0.5T \sim T$), particles originally in the lower portion of the vortex leg, e.g. the particles “1U” and “3C”, are significantly lifted up by the trailing vortex, while particles originally in the vortex head, e.g. the particles in group two, still remain close in the highly rotating vortex head, indicating a well-maintained coherence in the head even under the strong interaction.

3.3. Impact of Phase Differences

With the simulated colored fluid particles, three different vortical structures are observed at the four selected phase differences. At $\Delta\phi = \pi/2$ (Figure 7b), the two SJs merge together to form one combined vortex, which is much stronger than single hairpin vortices and can pass through the boundary layer quickly. At $\Delta\phi = 3\pi/2$ (Figure 7d), the two hairpin vortices are separate from each other without obvious interaction, forming two completely separated vortices. At $\Delta\phi = 0$ (Figure 7a) and π (Figure 7c), the legs of one hairpin vortex are entrained into the head of the other, forming partially interacting vortex structures. As such, the twin SJs have distinct vortex strengths at various phase differences, as revealed in the authors’ previous PIV experiments [23,24]. Furthermore, it is seen that, no matter which type of interaction occurs, the green particles issued from the downstream actuator are mainly scattered in the outer layer of the interacting structures, whereas the red particles issued from the upstream actuator are mainly enclosed inside. The different particle distributions can be caused by the different strengths of the vortical structures issued from the twin SJ actuators. The flow structures issued from the upstream actuator can hold vortical structures better than those from the downstream. Therefore, the particles issued from the upstream actuator are more concentrated inside of the interacting flow structures. This is especially so when the interacting structures develop into the second actuation period, as shown in the plane view of Figure 7a–c. It is also seen that at $\Delta\phi = 3\pi/2$ (Figure 7d), unlike its counterpart, the head of the SJ issued from the upstream actuator is not affected at all by the near-wall particles. All these observations support our previous statement, i.e., in any case, the SJ issued from the upstream actuator can better maintain its vortical structure than the SJ issued from the downstream actuator [23,24], and hence it dominates the interaction. The reason is obvious: the vortex produced by the upstream actuator has sufficient time to develop itself before the interaction, while the SJ issued from the downstream actuator is disturbed from the very beginning of its emergence.

The different capability of the two hairpin vortices in maintaining their own coherence can be further demonstrated in snapshots from the streamwise cross-section view. Figure 8 shows the snapshots from the $\Delta\phi = 0, \pi/2$ and π cases, at the same instant $t/T = 0$ as in Figure 7. In all three snapshots, the boundaries between the particles from different actuators are clear. At $\Delta\phi = \pi/2$ (Figure 8b), the head of the combined vortex includes two cores of fluid particles issued from the upstream actuator (in red) which are surrounded by scattered fluid particles issued from the downstream actuator (in green). At $\Delta\phi = 0$, the twin SJs produce partially interacting vortex structures (Figure 8a). The fluid particles issued from the upstream actuator still appear in two cores, forming the head of the trailing vortex, which is surrounded by the fluid particles issued from the downstream actuator. Moreover, two legs of the leading vortex with green particles appear near the mid-span

plane, whose induced flow pushes the upper portion of the trailing vortex heads (two red cores) away from each other, which is prominent if compared with the combined vortex head shown in Figure 8b. In the partially interacting vortex structures at $\Delta\phi = \pi$ (Figure 8c), the head of the trailing vortex (in green) no longer appears as two solid cores. Instead, it appears as two hollow tubes enclosing the two counter-rotating legs of the leading vortex with red particles, and its shape differs greatly from those in Figure 8a,b.

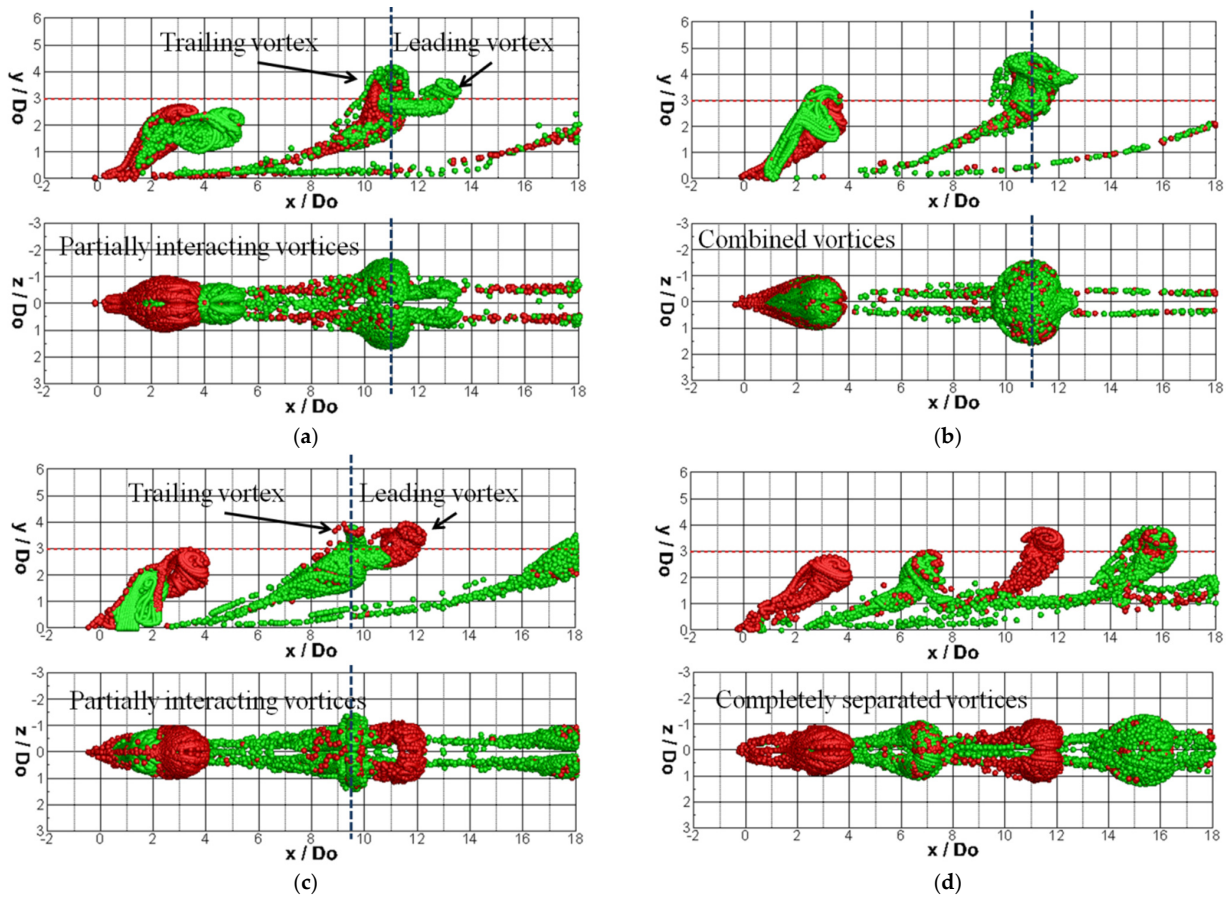


Figure 7. Colored fluid particles of the in-line twin SJs ($t/T = 0$), (a) $\Delta\phi = 0$, (b) $\Delta\phi = \pi/2$, (c) $\Delta\phi = \pi$, (d) $\Delta\phi = 3\pi/2$.

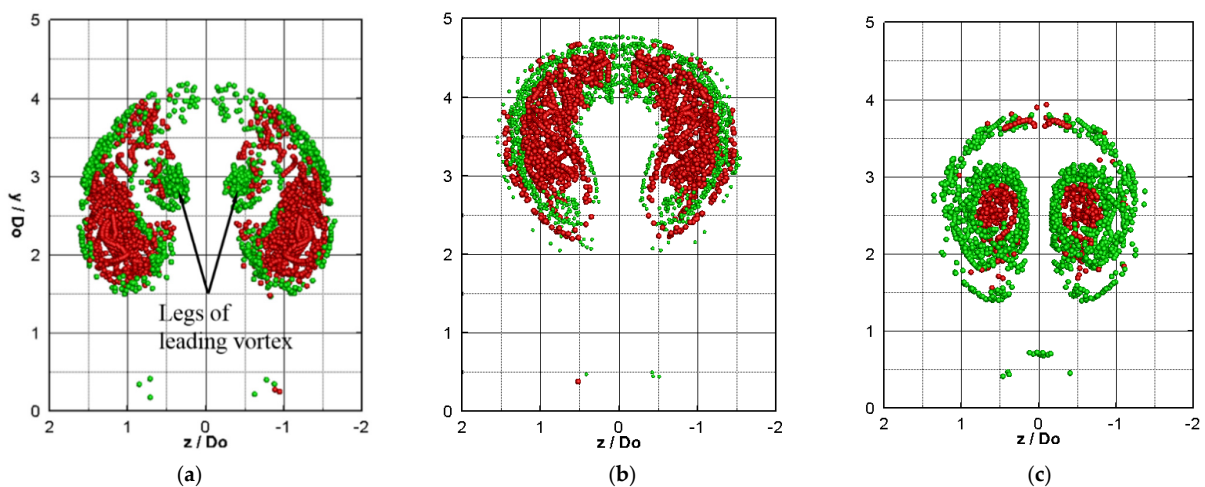


Figure 8. Snapshots of colored fluid particles from the streamwise cross-section view at (a) $x = 11D_o$ for the $\Delta\phi = 0$ case, (b) $x = 11D_o$ for the $\Delta\phi = \pi/2$ case and (c) $x = 9.5D_o$ for $\Delta\phi = \pi$ case ($t/T = 0$). These streamwise cross-section planes are indicated with dashed lines in Figure 7.

Particles issued from selected positions of the SJ actuator orifices are also tracked to study the interactions of SJ vortex structures, as shown in Figure 9. The single SJ and the twin SJs at $\Delta\phi = \pi/2$ and $3\pi/2$ are selected for presentation. Compared to those in the single SJ, the particles issued at the center of the orifices at $\Delta\phi = \pi/2$ are lifted to a much higher position at $x = 3D_o$ outside of the boundary layer. This is because a stronger vortex is merged from the twin SJs. The two particles issued from different actuators have strong interactions and rotate around the merged vortex head. In addition, the particles issued at $z/D_o = 0.4$ have a slightly faster rotation than that in a single SJ with a shorter traveling distance. On the other hand, the trajectories of particles at $\Delta\phi = 3\pi/2$ are similar to those in the single SJ because the two separated hairpin vortices are produced, with the exception that the particle issued at $z/D_o = 0.4$ from the downstream orifice is trapped in the tip of the hairpin leg with a straighter trajectory.

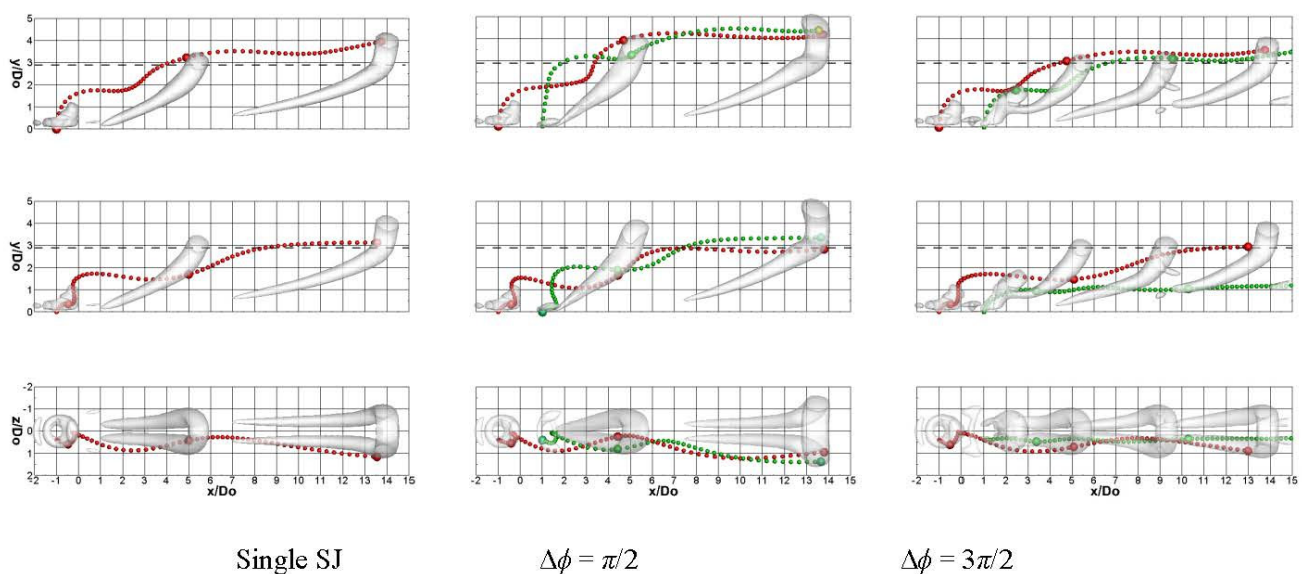


Figure 9. Tracking of particles that are released from different positions of the actuator orifices, top row: at center, middle & bottom rows: at $z/D_o = 0.4$ (side and plan views). Vortex structures are also added at $t/T = 0.25$ indicated by the particles with larger diameters.

Figure 10 shows the correlations of the streamwise and wall-normal velocity components at three selected stations in the mid-span plane. In the single-SJ case, the upwash flow of hairpin vortices can increase the velocity in the wall-normal direction and decrease the velocity in the streamwise direction in the boundary layer [23,24]. For the twin SJs at $\Delta\phi = \pi/2$, the disturbance of the boundary layer is much stronger, indicated by the larger correlation loop of the streamwise and wall-normal velocity components. The shape of correlation loop is similar to that in the single SJ, because only the stronger hairpin vortices are merged with similar vortex structures. On the other hand, the shape of the correlation loop becomes very different at $\Delta\phi = 3\pi/2$. At a phase difference of $\Delta\phi = 3\pi/2$, the SJ flow structures are produced alternately from the twin actuators with an almost equal time interval. Therefore, the twin SJs have a weak interaction but with a doubled frequency compared to single SJs. On the other hand, the twin SJs merge into a combined vortex at $\Delta\phi = \pi/2$ with a high strength but the same frequency to the single SJs. Differing from the single loop in the single-SJ case, two loops are observed with substantial differences. This indicates that the two separated hairpin vortices at $\Delta\phi = 3\pi/2$ also have notable differences in vortex strength. In addition, the smaller loops also imply that the hairpin vortices at $\Delta\phi = 3\pi/2$ are slightly weaker than that in the single-SJ case.

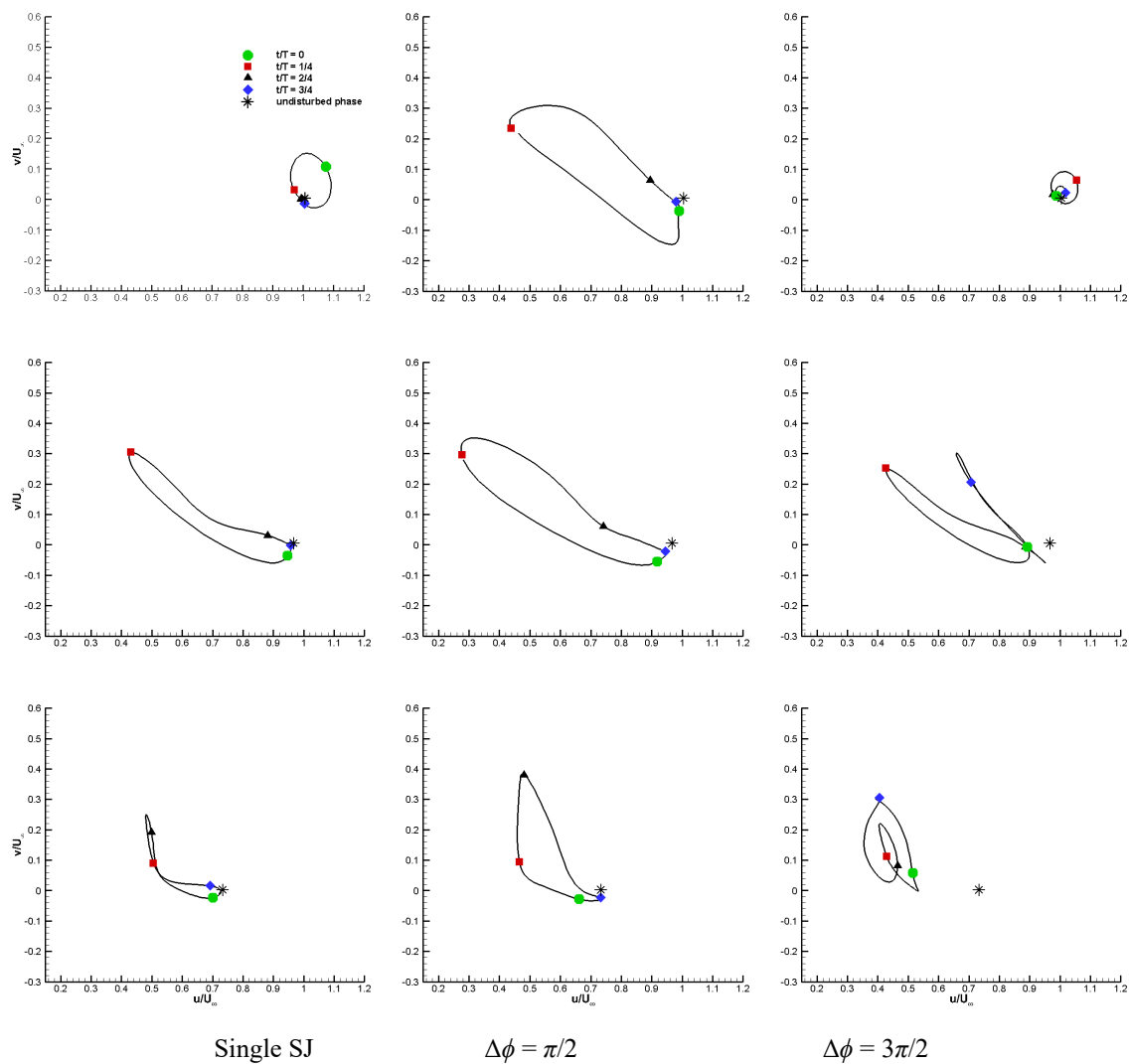


Figure 10. Correlations of streamwise and wall-normal velocity components in the mid-span plane at three selected positions, top: ($x = 5D_0$, $y = 3.4D_0$), middle: ($x = 5D_0$, $y = 2.4D_0$), bottom: ($x = 5D_0$, $y = 1.4D_0$).

4. Impact of SJ Vortices on Wall Shear Stress

Previous studies have revealed that the SJ-induced near-wall streamwise vortices, i.e., the hairpin legs and induced secondary vortices, play an important role in flow separation control or enhancement of heat and mass transfer [12]. In this section, in order to reveal details of the evolution of these streamwise vortices, iso-surfaces of a smaller value of $Q = 1$ are colored by streamwise vorticity. To examine the impact of the SJ vortices on the boundary layer, the excess wall shear stress is presented and calculated as $(\tau_w - \tau_{w, \text{nojet}}) / \tau_{w, \text{nojet}}$, which is a useful indicator of the SJ effectiveness in heat transfer enhancement [12].

4.1. Instantaneous Influence

Figure 11 shows the single-SJ-induced vortices and the corresponding contours of excess wall shear stress at the instant $t/T = 0$. Evolution of the primary hairpin vortices and secondary vortices has been discussed in our previous study [26]. These vortex structures influence the boundary layer as well as the wall shear stress. A pair of streaks of positive excess wall shear stress is observed outside of the SJs. This streak pair becomes wider near the regions between the legs of hairpin vortices and the secondary vortices (at about $8 < x/D_0 < 10$), where the downwash flow is strengthened by the interaction of the vortices.

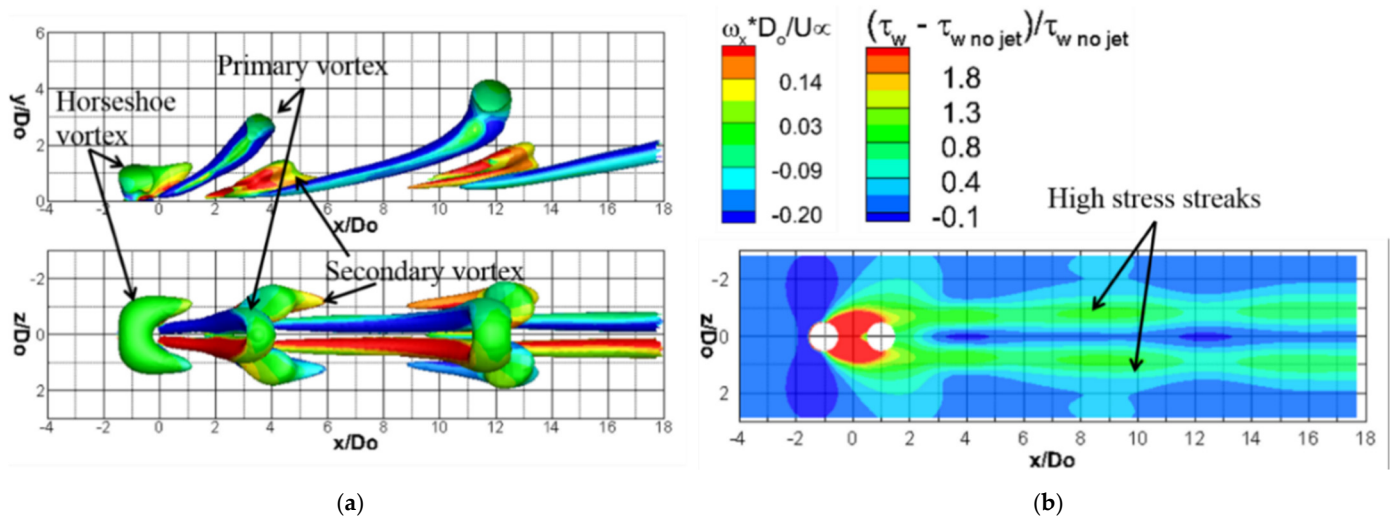


Figure 11. Vortex structures in the single-SJ case, captured using $Q = 1$ iso-surfaces (a) and excess wall shear stress (b) at $t/T = 0$.

The two SJs merge into a stronger vortex when their phase difference is $\Delta\phi = \pi/2$. As shown in Figure 12a, both the hairpin vortices and the induced vortices, including the secondary vortices and horseshoe vortex, become stronger compared to those induced by the single SJ. The evolution of these vortices presented in the upper two rows of Figure 12b reveals that, at $t/T = 0.25$ when the upstream SJ is at its maximum blowing, a vortex ring (labeled as A) is issued the upstream actuator. It lifts up the horseshoe vortex produced in the previous cycle. In the downstream part of this horseshoe vortex a pair of secondary vortices begin to form. At $t/T = 0.5$, the vortex ring A begins to evolve into a hairpin vortex due to its interaction with the crossflow. Meanwhile a new vortex ring (labeled as B) emerges at the downstream orifice, breaking the horseshoe vortex. In addition, the downstream secondary vortices become more obvious. At $t/T = 0.75$ & 1, the twin SJs combine into a stronger hairpin vortex, which is accompanied by stronger secondary vortices and a larger horseshoe vortex.

The enhancement of wall shear stress is more significant, especially near to the orifice ($x/D_o < 12$) in Figure 12a. However, the combined vortices are so strong that they quickly penetrate the boundary layer, resulting in significant decay of the excess wall shear stress in the far downstream. In addition, some deficit of the wall shear stress is found outboard of the secondary vortices, which is associated with the induced upwash flow [26]. Detailed examination in the near-orifice region shows that changing of the excess wall shear stress is obviously periodic during one actuation cycle, as shown in the bottom row of Figure 12b. At $t/T = 0.25$, besides the area around the upstream orifice, high excess wall shear stress is also found near the downstream orifice, which is induced by the legs of the preceding combined vortex and the associated secondary vortices. At $t/T = 0.5$, high excess wall shear stress is induced around the downstream orifice due to the emergence of the vortex ring B. The excess wall shear stress downstream of this orifice becomes weaker. At $t/T = 0.75$, as the two SJs begin to combine, the regions of high excess wall shear stress around the two orifices connect. At downstream of the orifices, a large area of negative excess wall shear stress forms between the new forming vortex and the preceding one. At $t/T = 1$, as the newly formed combined vortex convects downstream, positive excess wall shear stress recovers near the orifices.

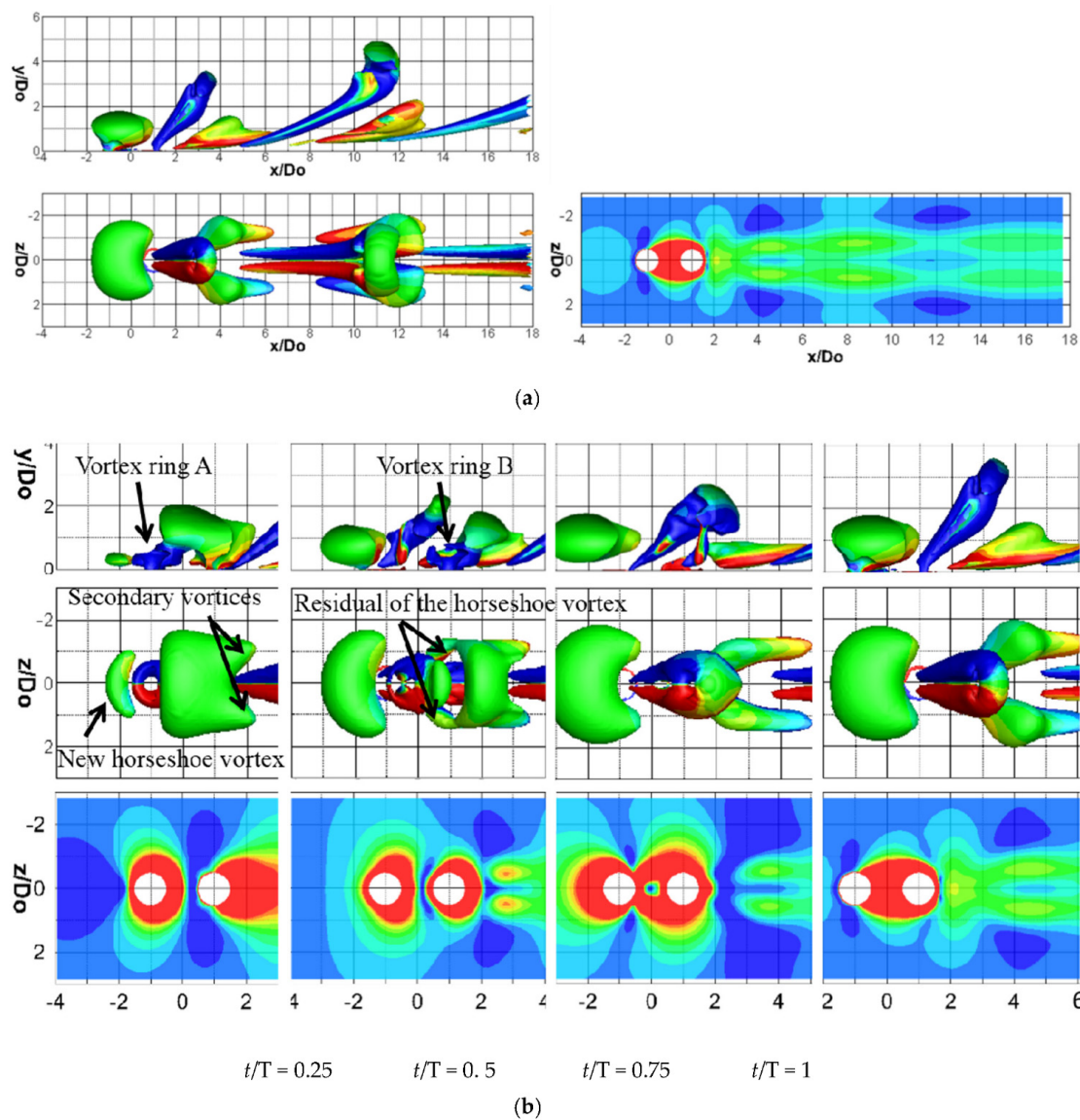


Figure 12. Vortex structures and excess wall shear stress for the twin SJs operating with $\Delta\phi = \pi/2$. (a) Vortex structures (left) and excess wall shear stress (right) at $t/T = 0$. (b) Evolution of vortices (upper two rows) and corresponding excess wall shear stress (bottom row). The color map can be referred to Figure 11.

Two completely separated vortices are produced at $\Delta\phi = 3\pi/2$. Primary hairpin vortex and outboard secondary vortices are induced as shown in left subplot of Figure 13a. However, their evolution processes start at different locations and instants. As shown in the upper two rows of Figure 13b, a pair of secondary vortices (labeled as #1) begins to form between the two orifices at $t/T = 0.25$. At $t/T = 0.5$, these secondary vortices become more obvious, as the horseshoe vortex is eliminated by the suction of the downstream actuator. They further grow at $t/T = 0.75$ and 1, and are sandwiched by the head of the SJ issued from the upstream actuator and the legs of the SJ issued from the downstream actuator. At $t/T = 1$, a vortex ring emerges from the downstream orifice and begins to evolve into a hairpin vortex at $t/T = 1.25$ (equivalently $t/T = 0.25$). By interacting with the preceding hairpin legs, it induces a pair of secondary vortices (labeled as #2) downstream. This pair of secondary vortices grows at $t/T = 1.5$ (equivalently $t/T = 0.5$), and finally becomes comparable to its counterpart (i.e., #1) at $t/T = 1.75$ (equivalently $t/T = 0.75$). Therefore, both the primary hairpin vortices and the induced secondary vortices double their appearance frequency (in other words, double their number) at far downstream. On

the other hand, they are all shorter than those in single SJ case. The strip pair of enhanced wall shear stress also reflects this doubled frequency, as shown in the right subplot of Figure 13a. The strips are narrower compared to single-SJ case. Also, due to the doubled frequency effect, the strips in the near-orifice region can maintain the high excess wall shear stress, as revealed in the bottom row of Figure 13b.

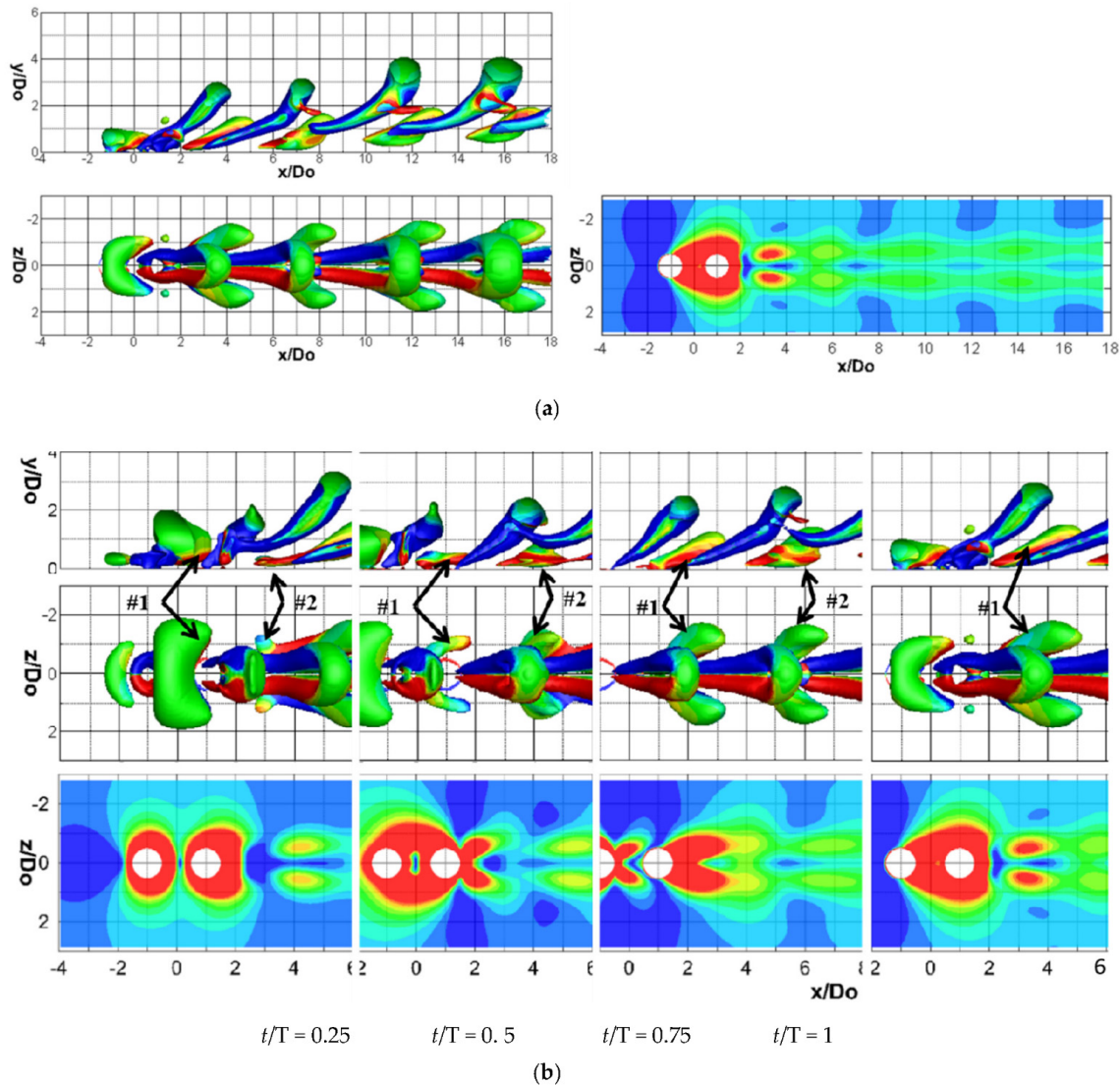


Figure 13. Vortex structures and excess wall shear stress for the twin SJs operating with $\Delta\phi = 3\pi/2$. (a) Vortex structures (left) and excess wall shear stress (right) at $t/T = 0$. (b) Evolution of vortices (upper two rows) and corresponding excess wall shear stress (bottom row). The color map can be referred to Figure 11.

Partially interacting vortex structures are produced at $\Delta\phi = 0$ and π . The Q iso-surfaces reveal that, no matter whether it is the trailing vortex (left subplot of Figure 14a) or leading vortex (left subplot of Figure 15a), the vortex produced from the upstream actuator dominates the interacting vortex structure in terms of vortex coherence. This is consistent to what has been revealed with the colored fluid particles in Section 3.3. For this reason, the vortex produced from the upstream actuator is also called the *dominant hairpin vortex* hereinafter, despite the phase difference. In both cases, a pair of much longer secondary vortices is induced by the interacting vortex structure, compared to the single-SJ case. Although appearing similar, these two partially interacting vortex structures show an interesting difference. That is, the lateral distance between the two legs of the partially

interacting SJs at $\Delta\phi = 0$ is much larger than that at $\Delta\phi = \pi$. This is because in both cases the legs of the interacting vortex structure are from the dominant hairpin vortex. At $\Delta\phi = 0$, the leading vortex is entrained through the gap between the legs of trailing dominant vortex. Therefore, the gap is enlarged during the process. On the other hand, at $\Delta\phi = \pi$, the legs of dominant leading vortex is pushed together by the trailing vortex, resulting in a smaller gap. This difference also affects the pattern of excess wall shear stress. Although the patterns in both cases are similar to that in the $\Delta\phi = \pi/2$ case in far downstream, the deficit in the centerline low stress region in the $\Delta\phi = 0$ case is significantly larger (right subplot of Figure 14a). Furthermore, at $\Delta\phi = 0$, the side view reveals that the legs of the dominant hairpin vortex are gradually “pulled” down toward the wall as the reaction to their entrainment of the leading hairpin legs, which are then able to exert more influence on the wall shear stress, especially in the far-downstream region. As such, the two high stress streaks in the mid- and far-downstream regions are stronger than those in the near-downstream region, which is quite different from what is observed in the other cases.

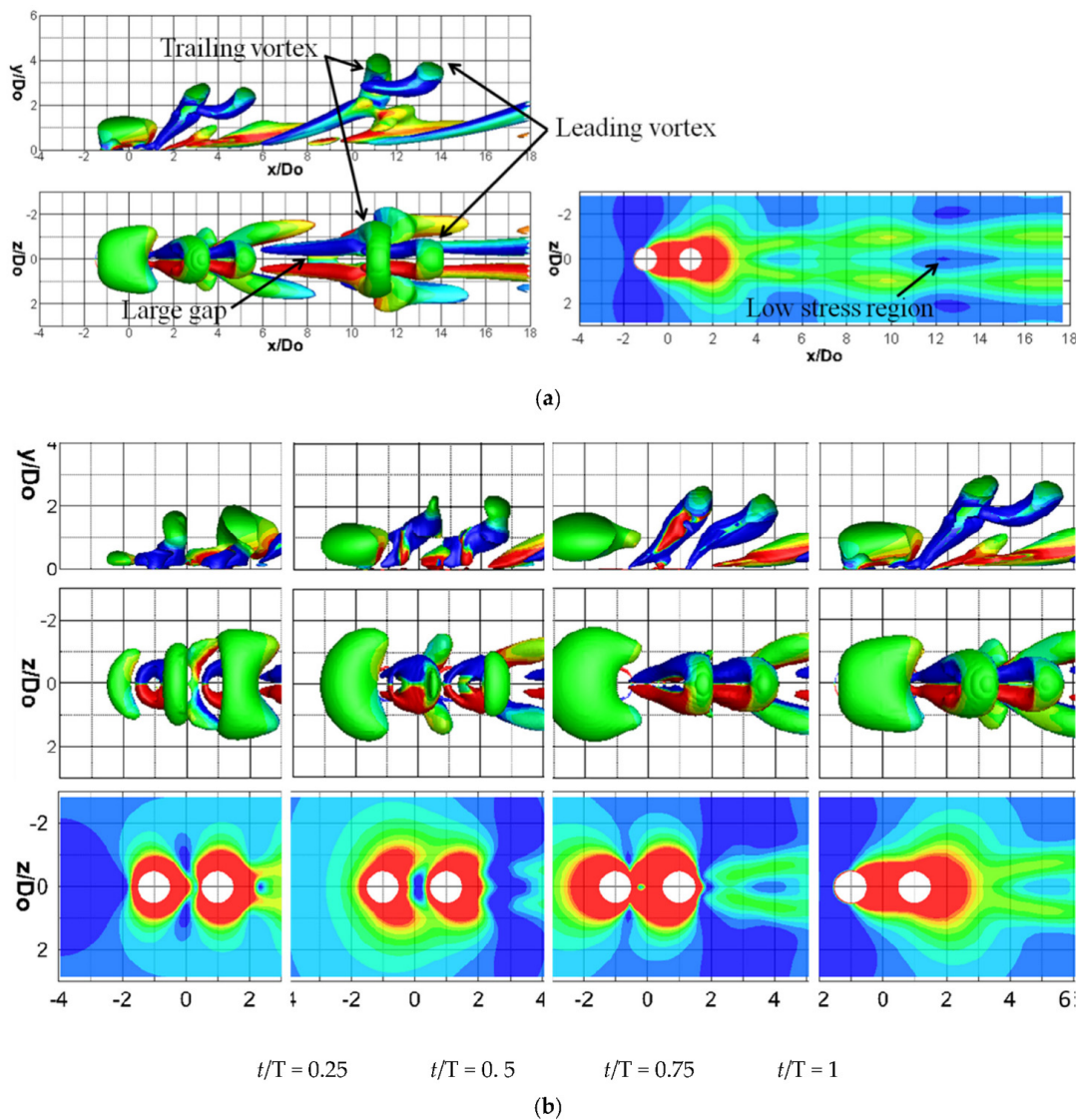


Figure 14. Vortex structures and excess wall shear stress for the twin SJs operating with $\Delta\phi = 0$. (a) Vortex structures (left) and excess wall shear stress (right) at $t/T = 0$. (b) Evolution of vortices (upper two rows) and corresponding excess wall shear stress (bottom row). The color map can be referred to Figure 11.

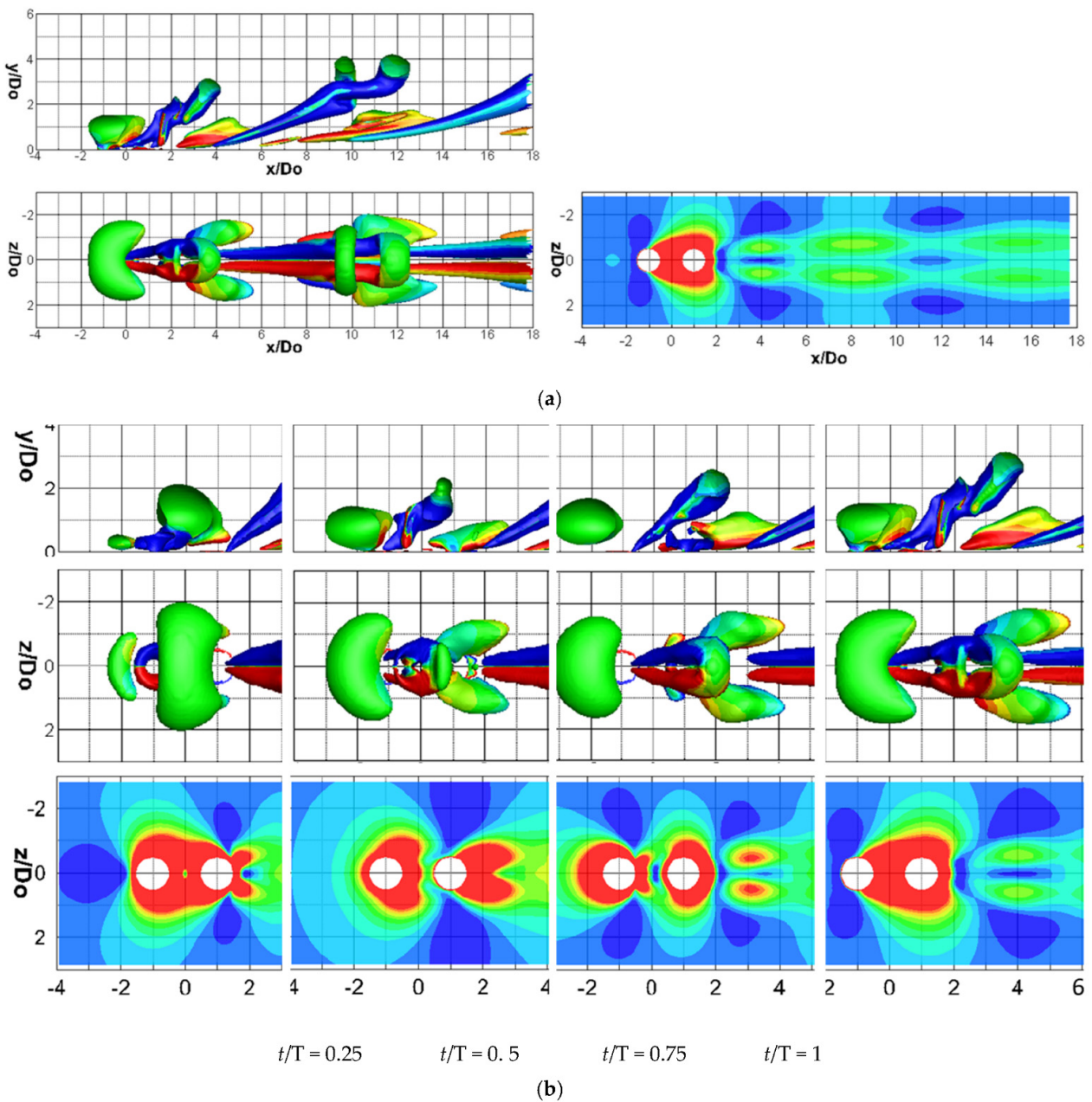


Figure 15. Vortex structures and excess wall shear stress for the twin SJs operating with $\Delta\phi = \pi$. (a) Vortex structures (left) and excess wall shear stress (right) at $t/T = 0$. (b) Evolution of vortices (upper two rows) and corresponding excess wall shear stress (bottom row). The color map can be referred to Figure 11.

4.2. Time-Averaged Influence

The time-averaged influence of the single and twin SJs on the wall shear stress is compared in Figure 16. It is seen that about $1D_o$ downstream of each operating actuator there exists an obvious region of negative excess stress, which is caused by the blockage of the SJs and the roll-up of the downstream branch of the SJ-induced vortex rings. Further downstream, the averaging removes the periodic patterns of the two streaks in all cases. Regardless the phase difference, the twin SJs can generate significantly more excess stress than the single SJ. But the persistency of the influence varies with phase difference. At $\Delta\phi = \pi/2$ the combined vortex structures induce a pair of wall shear stress streaks that is strong only within a short distance downstream from the orifices and starts decaying further downstream (see Figure 16c). This is because the combined vortices can penetrate

the boundary layer deeply. The vortices move away from the wall as they travel in the crossflow, resulting in a fast decaying influence on the wall in the far-downstream region. This is evidenced by the particle tracking (Figure 7b) and instant flow structures (Figure 12). On the contrary, at $\Delta\phi = 3\pi/2$ the two completely separated vortices can stay close to the wall (Figures 7d and 13), and produce a pair of high stress streaks that sustain their strength for a much longer distance. The partially interacting vortices at $\Delta\phi = 0$ induce two streaks of high wall shear stress with gradually increased strength as shown in Figure 11b, between which a much wider strip of low stress value is observed. However, the time averaged high stress streaks produced by the other partially interacting vortices at $\Delta\phi = \pi$ (Figure 16d) appears similar to that in the $\Delta\phi = \pi/2$ case.

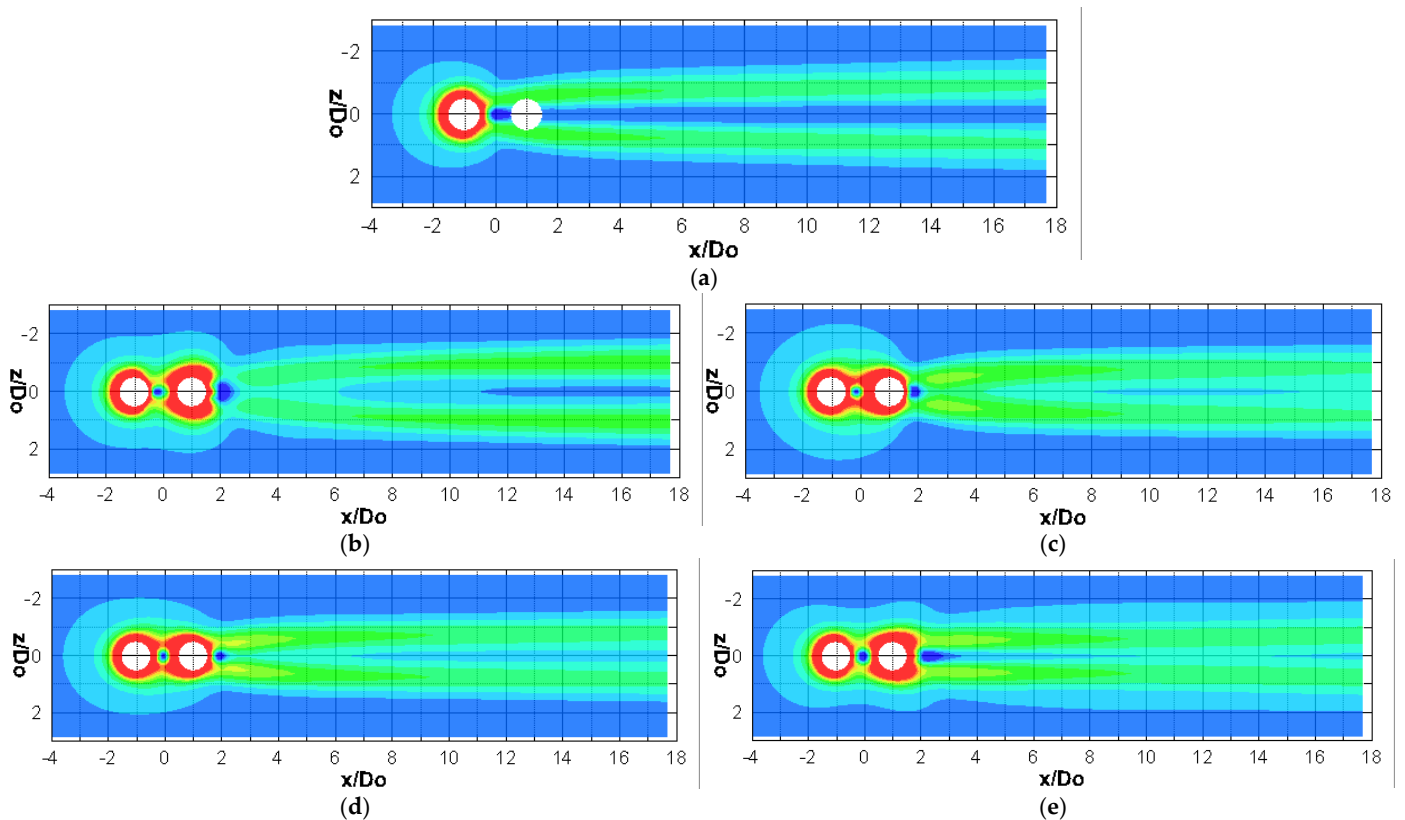


Figure 16. Time-averaged excess wall shear stress, (a) single SJ, (b) $\Delta\phi = 0$, (c) $\Delta\phi = \pi/2$, (d) $\Delta\phi = \pi$, (e) $\Delta\phi = 3\pi/2$. The color map can be referred to Figure 11.

In Figure 17, the excess wall shear stress is time-averaged and compared at two positions, i.e., $x = 4D_0$ and $18D_0$. In all cases, the two high stress streaks are represented by two peaks. At $x = 4D_0$, the two peaks induced by the single SJ are symmetrically located about $0.8D_0$ away from the mid-span plane, whereas the two peaks induced by all the twin SJs are slightly closer. It is also seen that the $\Delta\phi = 0$ case has a peak value close to that in the single SJ case. On the other hand, the other three twin SJ cases all have a much larger peak value (at least 20% higher). This is because in the $\Delta\phi = 0$ case the legs of the leading vortex (issued from the downstream actuator) are lifted up immediately after their emergence (as shown in Figures 6 and 7a), and hence the near-field wall shear stress is only affected by the legs of the trailing vortex (issued from the upstream actuator), while in the other three twin-SJ cases, i.e., $\Delta\phi = \pi/2$, π and $3\pi/2$, the near-field wall shear stress is affected by the legs of both vortices.

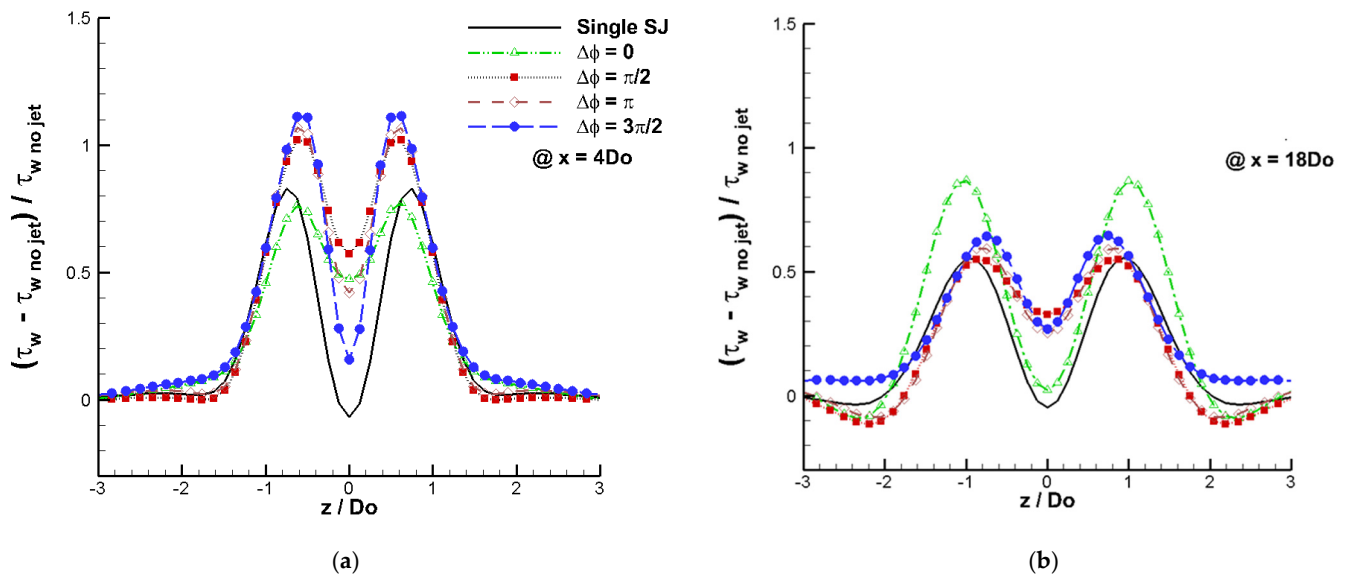


Figure 17. Time-averaged excess wall shear stress along spanwise direction at (a) $x = 4D_o$ and (b) $x = 18D_o$.

At $x = 18D_o$ that is far from the two orifices, due to the spreading of the vortex structures and their penetrating in the boundary layer, the two stress peaks in all cases are separated from each other with a larger distance, and, except for the $\Delta\phi = 0$ case, their peak values reduce quite significantly if compared with those at $x = 4D_o$. In the $\Delta\phi = 0$ case, wall shear stress gets larger as the flow structures traveling to downstream. This may be caused by the closer distance of the hairpin vortex to the wall and the increasing strength of the hairpin vortex during the merging process of the twin SJs. In addition, since the two legs of the dominant vortex is pushed away from each other by its counterpart vortex, the distance of the corresponding peaks becomes much larger than that in the other cases including the single SJ case. This is also consistent with what is observed in Figure 16. In addition, negative values of excess wall shear stress are also found at $x = 18D_o$ in $|z/D_o| > 2$ regions, except at $\Delta\phi = 3\pi/2$. From the instantaneous patterns of excess wall shear stress (Figures 12a, 14a and 15a), these negative values are ascribed to the deficit of wall shear stress outboard of the secondary vortices.

The excess wall shear stress is time-averaged, and then spanwise averaged within a range of $z = -1.6D_o \sim 1.6D_o$ where most of the non-zero excess stress is covered as revealed in Figure 17, and the streamwise distribution of the newly calculated quantity is then plotted and compared in Figure 18. It is seen that this time- and spatial-averaged excess stress in the single SJ case reaches a gentle peak at about $x = 3D_o$, and then decreases along the streamwise direction. In all the twin SJ cases, the curve begins with a significant rise, which corresponds to the region of negative excess stress right next to the downstream orifice as shown in Figure 16. Compared to the single SJ, in the $\Delta\phi = \pi/2$ case the combined vortex structures produce a peak of more than 40% larger at about $x = 3.5D_o$, after which the mean excess stress decreases with a higher rate, reaching a value of 26% larger at $x = 22D_o$. The trend is similar in the $\Delta\phi = 3\pi/2$ case where the two completely separated hairpin vortices are generated. Because of the doubling frequency effect in this case, the mean excess stress becomes almost unchanged after $x = 12D_o$, which turns to be larger than that in the $\Delta\phi = \pi/2$ case.

Although some difference is expected between the two cases that generate partially interacting vortex structures, it is still surprising to see a huge difference. The curve in the $\Delta\phi = \pi$ case follows a similar trend to that in the $\Delta\phi = \pi/2$ case, but with a slightly higher peak. But the curve in the $\Delta\phi = 0$ case varies quite differently: it reaches a plateau first at about $x = 4D_o$ where the excess stress is only 15% larger than that in the single SJ, and then increases further and reaches a gentle peak at about $x = 19D_o$ where the excess stress is

about 50% greater. This huge discrepancy stems from the difference in the evolution of the dominant vortex structure in these two cases. At $\Delta\phi = 0$, the legs of the dominant hairpin vortex are gradually “pulled” down toward the wall, which can exert stronger influence on the wall shear stress, especially in the far-downstream region.

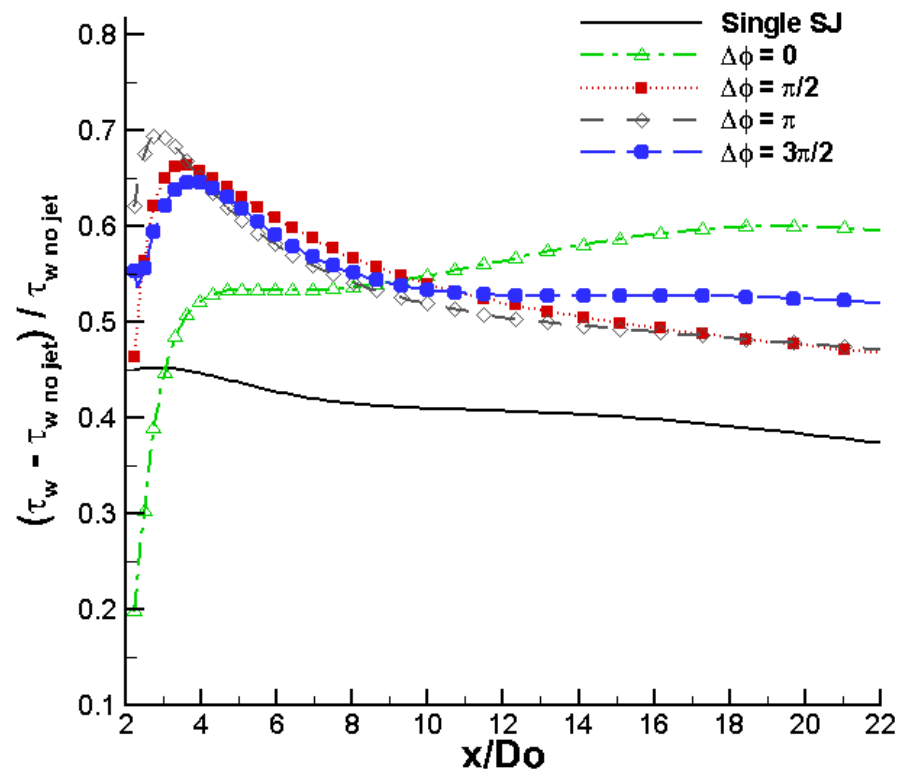


Figure 18. Mean excess wall shear stress along streamwise direction between $z = -1.6D_0 \sim 1.6D_0$.

5. Conclusions

The interaction of in-line twin SJs is examined in a laminar boundary layer numerically, that operate at various phase differences along a flat plate. Fluid particles of different colors released from the actuator orifices are tracked so as to show the mixing process of SJs in the boundary layer. In addition, the Q criterion is used to identify the twin SJ-induced vortex structures including both the primary and secondary vortices. The impact of these vortex structures on the boundary layer is also investigated through studying the excess wall shear stress. The major findings are as follows:

- (1) The fluid injected at the early stage of the blowing stroke mainly contributes to the formation of hairpin legs, the fluid injected near the maximum blowing mainly contributes to the formation of hairpin head, and the fluid injected at the late stage of the blowing stroke contributes very little to the formation of hairpin vortex because most of them are inhaled back into the actuator during the ingestion process.
- (2) When the twin SJs generate a *combined vortex* at $\Delta\phi = \pi/2$ or *partially interacting vortex structures* at $\Delta\phi = 0$ and π , fluid particles issued from the downstream actuator are mainly scattered in the outer layer of the interacting structures, whereas those issued from the upstream actuator are mainly enclosed inside. When the twin SJs generate *two completely separated hairpin vortices* at $\Delta\phi = 3\pi/2$, unlike its counterpart, the head of hairpin vortex issued from the upstream actuator is not affected at all.
- (3) The trajectories of selected particles reveal that the fluid particle near the hairpin head rotates about the center of the vortex head, whereas the fluid particle near the hairpin leg is trapped in the leg and travels downstream with a helix path.
- (4) The SJ-induced vortex structures make great impacts on the wall shear stress. In all cases a pair of streaks of positive excess wall shear stress can be observed. Although

both the $\Delta\phi = 0$ and $\Delta\phi = \pi$ cases produce partially interacting vortex structures, the induced two excess stress streaks are significantly different, which stems from the difference in the evolution of the vortex structures, especially of the dominant hairpin vortex, in these two cases.

Author Contributions: Writing—original draft preparation, H.W.; writing—review and editing, X.W.; supervision and project administration, D.X. and H.T.; methodology, L.L. and K.Z.; funding acquisition, X.W. All authors have read and agreed to the published version of the manuscript.

Funding: The authors gratefully acknowledge the financial support provided by the National Natural Science Foundation of China, China (grant Nos. 12072196) and the Science and Technology Commission of Shanghai Municipality, China (grant No. 19JC1412900), Advanced Jet Propulsion Innovation Center, China (AEAC HKCX2020-02-028), Aeronautical Science Foundation of China (2020Z006057001) and State Key Laboratory of Aerodynamics, China (SKLA-20200303).

Institutional Review Board Statement: Not applicable.

Informed Consent Statement: Not applicable.

Data Availability Statement: The data presented in this study are available on request from the corresponding author.

Conflicts of Interest: The authors declare no conflict of interest.

Nomenclature

D_o	orifice diameter, mm
D_d	diaphragm diameter, mm
d	actuator distance, mm
f	oscillation frequency, Hz
L	stroke length, mm
L_o	jet column length
p	pressure, Pa
Re_θ	momentum thickness
T	oscillation period, s
t	time, s
\bar{U}_o	jet velocity averaged over an entire actuation cycle, m/s
U_∞	bulk flow velocity, m/s
$u_o(t)$	instantaneous jet velocity, m/s
u_d	Diaphragm velocity, m/s
u_i	velocity, m/s
VR	velocity ratio
ν	viscosity, m^2s^{-1}
x_i	space location, mm
Δ	peak-to-peak displacement of the diaphragm, mm
δ	boundary layer thickness, mm
$\Delta\phi$	phase difference
ρ	fluid density, kg/m^3
τ_w	wall shear stress with control, Pa
$\tau_{w,nojet}$	wall shear stress without control, Pa
Acronyms	
SJ	synthetic jet
PIV	particle image velocimetry
CFD	computational fluid dynamics

References

- Smith, B.; Glezer, A. The formation and evolution of synthetic jets. *Phys. Fluids* **1998**, *10*, 2281. [[CrossRef](#)]
- Amitay, M.; Smith, D.R.; Kibens, V.; Parekh, D.E.; Glezer, A. Aerodynamic flow control over an unconventional airfoil using synthetic jet actuators. *AIAA J.* **2001**, *39*, 361–370. [[CrossRef](#)]

3. Amitay, M.; Glezer, A. Role of actuation frequency in controlled flow reattachment over a stalled airfoil. *AIAA J.* **2002**, *40*, 209–216. [[CrossRef](#)]
4. Liu, Y.H.; Tsai, S.Y.; Wang, C.C. Effect of driven frequency on flow and heat transfer of an impinging synthetic air jet. *Appl. Therm. Eng.* **2015**, *75*, 289–297. [[CrossRef](#)]
5. McGuinn, A.; Rylatt, D.I.; O'Donovan, T.S. Heat transfer enhancement to an array of synthetic air jets by an induced crossflow. *Appl. Therm. Eng.* **2016**, *103*, 996–1003. [[CrossRef](#)]
6. Luo, Z.B.; Deng, X.; Xia, Z.X.; Wang, L.; Gong, W.J. Flow field and heat transfer characteristics of impingement based on a vectoring dual synthetic jet actuator. *Int. J. Heat Mass Transfer* **2016**, *102*, 18–25. [[CrossRef](#)]
7. Xu, Y.; He, G.S.; Kulkarni, V.; Wang, J.J. Experimental investigation of influence of Reynolds number on synthetic jet vortex rings impinging onto a solid wall. *Exp. Fluids* **2017**, *58*, 6. [[CrossRef](#)]
8. Li, B.; Zhang, J.; Jiang, N. Influence of Synthetic Jets on Multiscale Features in Wall-Bounded Turbulence. *Actuators* **2022**, *11*, 199. [[CrossRef](#)]
9. Liu, J.-F.; Luo, Z.-B.; Deng, X.; Zhao, Z.-J.; Li, S.-Q.; Liu, Q.; Zhu, Y.-X. Dual Synthetic Jets Actuator and Its Applications—Part II: Novel Fluidic Thrust-Vectoring Method Based on Dual Synthetic Jets Actuator. *Actuators* **2022**, *11*, 209. [[CrossRef](#)]
10. Zhong, S.; Millet, F.; Wood, N. The behaviour of circular synthetic jets in a laminar boundary layer. *Aeronaut. J.* **2005**, *109*, 461–470. [[CrossRef](#)]
11. Jabbal, M.; Zhong, S. The near wall effect of synthetic jets in a boundary layer. *Int. J. Heat Fluid Flow* **2008**, *29*, 119–130. [[CrossRef](#)]
12. Jabbal, M.; Zhong, S. Particle image velocimetry measurements of the interaction of synthetic jets with a zero-pressure gradient laminar boundary layer. *Phys. Fluids* **2010**, *22*, 063603. [[CrossRef](#)]
13. Lee, A.; Timchenko, V.; Yeoh, G.H.; Reizes, J.A. Three-dimensional modelling of fluid flow and heat transfer in micro-channels with synthetic jet. *Int. J. Heat Mass Transfer* **2012**, *55*, 198–213. [[CrossRef](#)]
14. Lee, A.; Yeoh, G.H.; Timchenko, V.; Reizes, J.A. Heat transfer enhancement in micro-channel with multiple synthetic jets. *Appl. Therm. Eng.* **2012**, *48*, 275–288. [[CrossRef](#)]
15. Watson, M.; Jaworski, A.; Wood, N. Contribution to the understanding of flow interactions between multiple synthetic jets. *AIAA J.* **2003**, *41*, 747–749. [[CrossRef](#)]
16. Liddle, S.; Crowther, W.; Wood, N. Investigation of phase and spacing effects in synthetic jet actuator arrays. In Proceedings of the 43rd AIAA Aerospace Sciences Meeting and Exhibit, Reno, NV, USA, 10–13 January 2005; p. 107.
17. Liddle, S.; Wood, N. Investigation into clustering of synthetic jet actuators for flow separation control application. *Aeronaut. J.* **2005**, *109*, 35–44. [[CrossRef](#)]
18. Honami, S.; Motosuke, M. Vortex interaction of in-line synthetic jets injected at difference phase in low Reynolds number cross flow. In Proceedings of the 6th AIAA Flow Control Conference, New Orleans, LA, USA, 25–28 June 2012; p. 243.
19. Haller, G.; Yuan, G. Lagrangian coherent structures and mixing in twodimensional turbulence. *Phys. D Nonlinear Phenom.* **2000**, *147*, 352–370. [[CrossRef](#)]
20. Shadden, S.C.; Lekien, F.; Marsden, J.E. Definition and properties of Lagrangian coherent structures from finite-time Lyapunov exponents in two-dimensional aperiodic flows. *Phys. D* **2005**, *212*, 271–304. [[CrossRef](#)]
21. Franco, E.; Pekarek, D.N.; Peng, J.; Dabiri, J.O. Geometry of unsteady fluid transport during fluid–structure interactions. *J. Fluid Mech.* **2007**, *589*, 125–145. [[CrossRef](#)]
22. Hunt, J.; Wray, A.; Moin, P. Eddies, streams, and convergence zones in turbulent flows. In Proceedings of the 1988 Summer Program, Center for Turbulence Research, Stanford University, Stanford, CA, USA, 1 December 1988; pp. 193–208.
23. Wen, X.; Tang, H.; Duan, F. Vortex dynamics of in-line twin synthetic jets in a laminar boundary layer. *Phys. Fluids* **2015**, *27*, 083601. [[CrossRef](#)]
24. Wen, X.; Tang, H. Dye visualization of in-line twin synthetic jets in crossflows—A parametric study. *ASME J. Fluids Eng.* **2017**, *139*, 091203. [[CrossRef](#)]
25. Tang, H.; Zhong, S. Incompressible flow model of synthetic jet actuators. *AIAA J.* **2006**, *44*, 908–912. [[CrossRef](#)]
26. Wen, X.; Tang, H. On hairpin vortices induced by circular synthetic jets in laminar and turbulent boundary layers. *Comput. Fluids* **2014**, *95*, 1–18. [[CrossRef](#)]
27. Zhou, J.; Zhong, S. Numerical simulation of the interaction of a circular synthetic jet with a boundary layer. *Comput. Fluids* **2009**, *38*, 393–405. [[CrossRef](#)]
28. Anderson, W.K.; Bonhaus, D.L. An implicit upwind algorithm for computing turbulent flows on unstructured grids. *Comput. Fluids* **1994**, *23*, 1–21. [[CrossRef](#)]
29. Tafarojnoruz, A.; Gaudio, R. Vortex scouring process around bridge pier with a caisson. *J. Hydraul. Res.* **2012**, *50*, 443–444. [[CrossRef](#)]
30. Calomino, F.; Tafarojnoruz, A.; De Marchis, M.; Gaudio, R.; Napoli, E. Experimental and Numerical Study on the Flow Field and Friction Factor in a Pressurized Corrugated Pipe. *J. Hydraul. Eng.* **2015**, *141*, 04015027. [[CrossRef](#)]
31. Tafarojnoruz, A.; Lauria, A. Large eddy simulation of the turbulent flow field around a submerged pile within a scour hole under current condition. *Coast. Eng. J.* **2020**, *62*, 489–503. [[CrossRef](#)]